Experimental and Theoretical Study on Well-Tunable Metal Oxide Doping towards High-Performance Thermoelectrics

Enzheng Shi,[1,2#] Tianli Feng,[3#] Je-Hyeong Bahk,[4] Yu Pan,[5,6] Wei Zheng,[1] Zhe Li,[1] G. Jeffery Snyder,[6] Sokrates T. Pantelides[3] and Yue Wu[1,2*]

Most existing thermoelectric materials exhibit high performance only within a narrow temperature window. Among them, bismuth antimony telluride (BiSbTe) is a typical p-type thermoelectric material working near room temperature, but its performance decays rapidly with increasing temperature mainly due to the bipolar thermal transport. Suppressing bipolar thermal transport normally requires a delicate manipulation of band structure, possibly achievable through well-engineered extrinsic doping. Here we present a straightforward approach to dope BiSbTe with earth-abundant CuO. Different from embedding CuO nanoparticles that were extensively reported in literature, we observed that Cu and O atoms dissociate after spark plasma sintering. Density-functional-theory calculations reveal that it is the substitutional Cu at Sb/Bi sites and the interstitial O impurities that induce holes and increase carrier concentration as well as the power factor. The increase of hole concentration strongly suppresses the bipolar thermal conductivity. To the best of our knowledge, this is the first theoretical demonstration of p-doping of bismuth telluride thermoelelctrics from oxygen. Meanwhile, the Cu defects and O impurities strongly suppress the lattice thermal conductivity. As a result, the obtained material possesses optimized zT over a much wider temperature range with well-controllable peak temperature as a function of CuO concentration.

[1]*Department of Chemical and Biological Engineering, Iowa State University, Ames, IA 50011, USA*
[2]*Ames Laboratory, Department of Energy, Ames, IA 50011, USA*
[3]*Department of Physics and Astronomy and Department of Electrical Engineering and Computer Science, Vanderbilt University, Nashville, TN 37235, USA*
[4]*Department of Mechanical and Materials Engineering, University of Cincinnati, Cincinnati, OH 45221, USA*
[5]*State Key Laboratory of New Ceramics and Fine Processing, School of Materials Science and Engineering, Tsinghua University, Beijing 100084, P. R. China*
[6]*Department of Materials Science and Engineering, Northwestern University, Evanston, IL 60208, USA*
E-mail: *yuewu@iastate.edu. #These authors contributed equally*

Thermoelectric (TE) materials can convert waste heat into electricity as well as realize solid-state cooling. The performance of TE materials is evaluated by a dimensionless figure of merit zT, which is defined as $zT=\sigma S^2 T/\kappa_{tot}$, where σ is the electrical conductivity, S is the Seebeck coefficient, T is the absolute temperature, and κ_{tot} is the total thermal conductivity. The κ_{tot} is the sum of unipolar electronic κ_e, lattice κ_{lat}, and bipolar κ_{bi}. Many materials with high zT values are under investigation. However, most of these materials possess high zT values only within a very narrow temperature range, which significantly limits potential applications by the obligation to stack multiple materials either in parallel or in series to cover a wide temperature range. Inter-diffusion, thermal interface resistance, and thermal expansion stress reduce the reliability of the TE system. Using bismuth telluride (Bi_2Te_3)-based materials as examples, they are among the best and most widely explored TE materials near room temperature.[1-3] The modulation of the thermoelectric performance of Bi_2Te_3-based materials can be realized by defect engineering and band tailoring methods.[4-9] For example, phonon engineering is the primary strategy to control the lattice thermal conductivity.[10-12] To suppress the pronounced bipolar effect in Bi_2Te_3-based materials at elevated temperatures, extrinsic doping (using metal elements, metal telluride and selenide, Bi or Sb halide) can be adopted to adjust the Fermi level to tune the carrier concentration, thereby effecting the σ, S and κ_{tot}.[13-18] Moreover, as one important class of thermoelectric materials, metal oxides have also drawn significant attention.[19-22] However, compared with Bi_2Te_3-based materials, oxide thermoelectric materials have lower carrier mobilities, higher κ_{lat}, and larger bandgaps, restricting their zT values far below 1.0, while peaking at relatively high temperatures.[19,20] To the best of our knowledge, the application of metal-oxide doping in the Bi_2Te_3-based materials, which may result in a boost of the thermoelectric performance, has never been explored, although it was reported that metal oxide nanopowders could be embedded as nanoinclusions to improve the thermoelectric performance.[23-25]

Indeed, many controversial mechanisms of Cu doping in Bi_2Te_3-based materials have been reported in the past,[13,26-28] as most of them claimed Cu as a p-type dopant yet a few claimed it n-type. While Cu doping remains unclear, O doping in these materials has never been reported yet and the mechanism is unknown. The possibility that Cu impurities are good p-type dopants, i.e., they introduce excess holes in Bi_2Te_3-based materials, has been invoked in the past on the grounds that Cu substitutes Bi^{3+} or Sb^{3+} in a +2 oxidation state.[13] Such arguments,

however, have a high degree of uncertainty for impurities that do not come from a column to the immediate left of the host-atom column in the periodic table because there is a substantial likelihood that the defect potential is strong and introduces deep localized levels in the energy gap. To complicate matters further, Bi_2Te_3-based materials have very small energy gaps so that experience from conventional semiconductors, which typically have larger energy gaps, does not provide adequate guidance. No direct experimental evidence or theoretical calculations have been reported so far in support of Cu being a p-type or n-type dopant in Bi_2Te_3-based materials. Oxygen obviously is isoelectronic with Te so that it is not expected to dope either n-type or p-type, if it substitutes one of these two elements. Again, the very small energy gap and the strength of the oxygen potential disallow any definitive conclusions from general considerations.

In this work, we demonstrate a new approach to dope BiSbTe by earth abundant CuO and find that CuO dissociates with Cu dopants tending to partially segregate and O dopants remaining dispersed. CuO of as low as 0.05 %~0.3 % concentration shows an unambiguous p-type

doping effect which increases the electrical conductivity and significant-ly suppresses the bipolar effect, yielding a comprehensively pronounced zT (above 1.0) functioning from 313 K to 514 K compared with the pure BiSbTe counterpart. In addition, an excellent controllability of the zT peak temperature by varying the CuO concentration demonstrates the capability of the doped BiSbTe materials in a wide temperature range. Boltzmann-transport-equation (BTE) and first-principles density-functional-theory (DFT) modeling are performed to evaluate the contributions from grain size and CuO concentration and to identify the p-type doping from both Cu and O. Specifically, we demonstrate that substitutional Cu at both Sb and Bi sites and interstitial oxygen act as p-type dopants.

Fine commercial $Bi_{0.5}Sb_{1.5}Te_3$ powders (400 mesh, American Elements) were mixed with CuO nanopowders (<50 nm, Sigma Aldrich), followed by a ball-milling process, resulting in a uniform mixture of BiSbTe and x%CuO (x% represents the weight ratio of CuO in the composite). As shown in Fig. 1a, the BiSbTe·x%CuO powders were loaded into a graphite die (Φ=10.5 mm) and sealed by two punches so that the
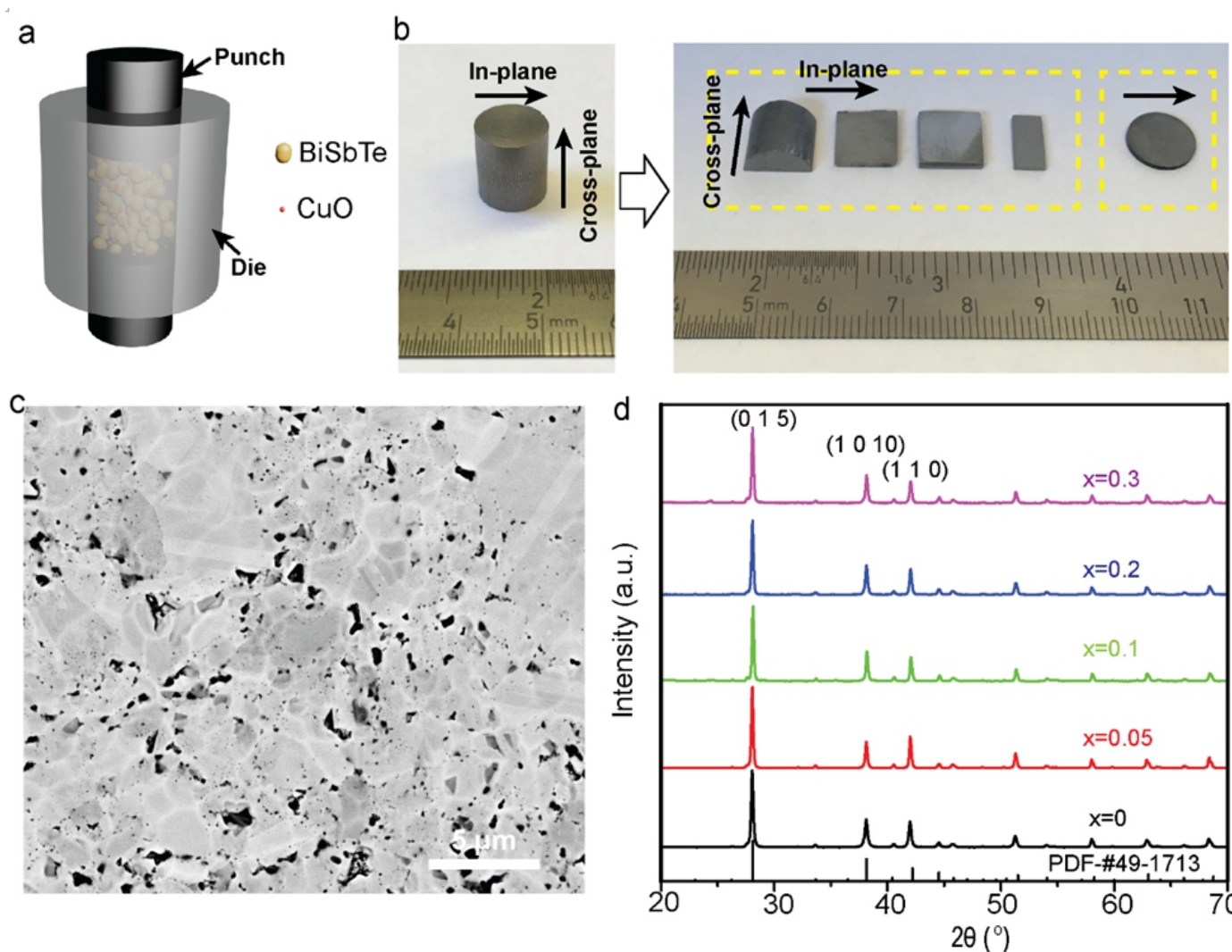

Fig. 1 Characterization of BiSbTe·x%CuO composites. (a) Schematic image of loading the mixture of BiSbTe powder and CuO nanoparticles into graphite die and punches for SPS; (b) Photo images of BiSbTe·x%CuO composites; the left image represents the as-sintered cylindrical sample and the right one corresponds the disk and bars cut from the left tall cylinder; (c) Back-scattering SEM image of BiSbTe·0.3%CuO sample; (d) XRD patterns of BiSbTe·x%CuO composites; The peaks are well matched with the standard hexagonal single phase $Bi_{0.5}Sb_{1.5}Te_3$ (PDF-#49-1713 represents standard $Bi_{0.5}Sb_{1.5}Te_3$ phase).

pressure could be exerted uniaxially. After spark plasma sintering(SPS), a cylinder sample with a height of ~12 mm (the left photo image in Fig. 1b) was obtained. The density of the as-sintered composites was determined to be around 6.70~6.73 g/cm³, 97.4 %~97.8 % of the theoretical value. To measure the thermoelectric properties along the in-plane and cross-plane directions respectively, the BiSbTe·x%CuO cylinder was diced into several parts (Fig. 1b). The left parts (labeled by the wide dashed yellow rectangle) were used to measure the cross-plane electrical conductivity (σ), Seebeck coefficient (S) and in-plane thermal conductivity (κ_{tot}), while the right disk was used to measure the in-plane σ, S and cross-plane κ_{tot}. All the following thermoelectric properties and characterizations discussed in the main text are along cross-plane direction. The in-plane thermoelectric properties were found to have similar thermoelectric performance as shown in Fig. S1. From the scanning electron microscopy (SEM, Fig. 1c and Fig. S2) images of BiSbTe·0.3%CuO and BiSbTe samples, plenty of tiny pores are included in the composite. And the grain size ranges from tens of nanometers to several micrometers, consistent with the TEM images (Fig. S3). The hierarchical architecture with broad grain size distribution as well as the nanosized pores helps suppress the lattice thermal conductivity due to scattering phonons of different frequencies.[29-31] The matrix phase was identified as $Bi_{0.5}Sb_{1.5}Te_3$ (PDF-#49-1713) according to the X-ray diffraction (XRD) patterns (Fig. 1d). Due to the low CuO concentration (0.05 % to 0.3 %), no secondary phase was recognized from the XRD patterns.

After the SPS process, the thermoelectric properties of BiSbTe·x%CuO composites were measured. Fig. 2 demonstrates the temperature-dependent electrical conductivity, Seebeck coefficient, and power factor of BiSbTe·x%CuO composites with different CuO concentrations x%. We performed carrier transport modeling based on the linearized Boltzmann transport equation to fit the experimental data and added the fitting curves in Fig. 2. The theoretical model shows an excellent fitting with the experimental data. Detailed information about the modeling can be found in the Supplemental Information (Part 3.1) and Ref.[32] As shown in Fig. 2a, with the increase of CuO concentration x%, σ increases fourfold from 0.32×10^5 S/m (pure BiSbTe) to 1.63×10^5 S/m (BiSbTe·0.3%CuO) at 317 K, implying an effective doping by CuO incorporation. For pure BiSbTe samples, there is a continuous decrease of σ when measured from 300 K to 436 K, which is a typical characteristic of degenerate semiconductors, in which the carrier concentration remains constant and the mobility decreases with temperature due to increased phonon scattering. However, σ begins to increase after the

temperature exceeds 436 K for pure BiSbTe, due to the increased minority carriers (bipolar effect). In comparison, the bipolar effect for the BiSbTe·x%CuO composites is effectively suppressed and σ decreases monotonically over the entire measurement temperature range (from 300 to 520 K).

The positive Seebeck coefficient S indicates that the BiSbTe·x%CuO composites are p-type semiconductors (Fig. 2b). Different from σ, S is negatively correlated with the carrier concentration,[7,33] hence the pure BiSbTe sample possessed larger S compared with the BiSbTe·x%CuO composites before intrinsic excitation (when the temperature was lower than 440 K). The maximum S (S_{max}) for the pure BiSbTe sample reaches 279 µV/K at 334 K, while S_{max} is lowered to 238 µV/K at 367 K for BiSbTe·0.05%CuO, and to 209 µV/K at 474 K for BiSbTe·0.1%CuO, respectively. For BiSbTe·0.2%CuO and BiSbTe·0.3%CuO composites, the temperature for S_{max} is beyond the measurement temperature (larger than 514 K). Therefore, S_{max} decreases with x, while the temperature for S_{max} increases with x. With the climbing of the measurement temperature, the S value of BiSbTe·x%CuO gradually exceeds that of the pure BiSbTe sample, yielding larger powder factors (PF) for BiSbTe·x%CuO composites (Fig. 2c). This probably leads to a pronounced zT at higher temperature after CuO doping. Additionally, the PF of BiSbTe·x%CuO composites are larger than the pure BiSbTe sample, in which the PF for the BiSbTe·0.3%CuO and pure BiSbTe composites are 2.26 and 0.72 mW/(m·K²) at 514 K respectively.

As revealed above, due to the effective doping, small concentrations of CuO enhance the electrical conductivity of p-type BiSbTe nanocomposites significantly. Hall-effect measurements were performed to study the doping effect of CuO, from which the Hall carrier concentration n_H and mobility μ_H were extracted (Fig. S6). As the bipolar conduction is not significant at low temperature (e. g. 313 K), the n_H for all the BiSbTe·x%CuO composites (including pure BiSbTe samples) is mostly contributed by the majority carriers, i. e. holes. Due to the effective doping by CuO, n_H increases from 9.17×10^{18} cm⁻³ for the pure BiSbTe sample to 5.77×10^{19} cm⁻³ for BiSbTe·0.3%CuO sample. Also, the resulting mobility of the majority carriers (holes) as a function of temperature is obtained from the transport modeling, as is shown in Fig. S6b. The mobility steadily decreases with increasing CuO concentration due to the increased impurity scattering.

Annular dark-field imaging (HAADF) scanning transmission electron microscope (STEM) and energy dispersive spectroscopy (EDS) elemental mapping were utilized to study the solubility of CuO inside the
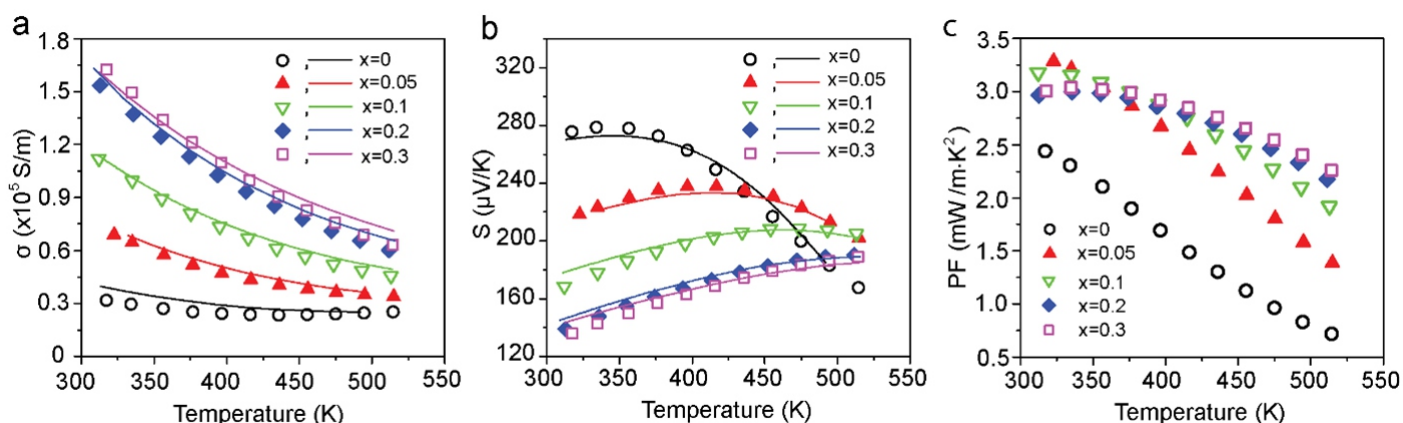

Fig. 2 Thermoelectric performance of BiSbTe·x%CuO. Electrical conductivity (σ, a), Seebeck coefficient (S, b) and power factor (PF, c) of BiSbTe·x%CuO with different CuO concentration x. Symbols are experimental data and the continuous curves are theoretical fittings based on the carrier transport modeling in (a) and (b).

BiSbTe matrix. The diameter of commercial CuO nanoparticles is 20~50 nm (Sigma-Aldrich), verified by the TEM image (Fig. S4). From the HAADF-STEM image and EDS mapping for the BiSbTe·0.3%CuO sample (Fig. 3), the Cu enrichment area has a size of ~47 nm, which matches the diameter of CuO nanoparticle very well. This also implies that Cu is not completely doped into BiSbTe. However, no oxygen enrichment is observed, suggesting that the oxygen is uniformly distributed inside the BiSbTe matrix.

The thermal conductivity κ_{tot} was measured by the laser-flash method. As was indicated from the temperature-dependent κ_{tot} in Fig. 4a, κ_{tot} ranges from 0.8 to 1.4 W/(m·K). With an increase of the concentration of CuO, κ_{tot} increases from 0.84 to 1.33 W/(m·K) at about 313 K, which is mainly contributed by the increase of the electronic thermal conductivity κ_e. The determination of κ_e is based on the Wiedemann-Franz law $\kappa_e = L\sigma T$, where L represents the Lorenz number. The calculation of L was performed using BTE modeling, as described in the Supplemental Information, and the temperature-dependent of L is shown in Fig. S5. As shown in Fig. 4b, κ_e increases with the CuO amount across the entire measurement temperature range, which is consistent with the trend of σ with CuO amount (Fig. 2a). As the CuO can significantly enhance σ, κ_e for BiSbTe·0.3%CuO is as large as 0.69 W/(m·K) at 313 K, while that of pure BiSbTe is only 0.15 W/(m·K). κ_{tot} can be expressed as $\kappa_e + \kappa_{bi} + \kappa_{lat}$. Based on our XRD spectra, SEM and TEM images (Fig. 1c, Fig. S3 and Fig. S4), the average grain size of BiSbTe is approximately 1 μm. By considering the grain size (related to the grain boundaries) and other defects in our BiSbTe·x%CuO

composites including the antisite and interstitial defects, the simulation of κ_{lat} was performed via the phonon Boltzmann transport equation including all the phonon branches with the full dispersions shown in Fig. S7 obtained from first-principles DFT calculations. Compared with BiSbTe alloys, the 1 μm grain size leads to a reduced κ_{lat} from 0.82 W/(m·K) to 0.67 W/(m·K) for our pure BiSbTe composite (Fig. S8). With increasing CuO concentration, κ_{lat} is slightly reduced due to the increased phonon scattering induced by Cu and O (Fig. S9). However, the impact of CuO in the reduction of κ_{lat} is not significant due to the low concentration of CuO (the maximum concentration herein as only 0.3 %). The simulation shows that κ_{lat} can be further reduced by increasing the CuO concentration. The simulated κ_{lat} at 300 K is 0.67 W/(m·K) for pure BiSbTe sample and decreases to 0.62 W/(m·K) for the BiSbTe·0.3%CuO sample, as presented in Fig. 4c and Fig. S9. In addition, by subtracting κ_e from κ_{tot}, we obtained the temperature-dependent of $\kappa_{tot} - \kappa_e$ (Fig. 4c). It is notable that the calculated κ_{lat} agrees well with $\kappa_{tot} - \kappa_e$ initially at 313 K. With the increase of temperature, $\kappa_{tot} - \kappa_e$ gradually surpasses κ_{lat}. The discrepancy between them comes from the bipolar contribution, which becomes important when the concentration of minority carriers (electrons) increases, thus increasing the κ_{tot}. Compared with the slight difference in κ_{bi}, the $\kappa_{tot} - \kappa_e$ (i.e. $\kappa_{bi} + \kappa_{lat}$) shows a decreasing tendency with increasing CuO concentration. This result demonstrates that Cu and O doping can efficiently suppress the bipolar contribution. The κ_{bi} for the pure BiSbTe sample increases continuously with temperature from 0.04 W/(m·K) at 313 K to about 0.70 W/(m·K) at 492 K, while κ_{bi} for the BiSbTe·0.3%CuO sample is
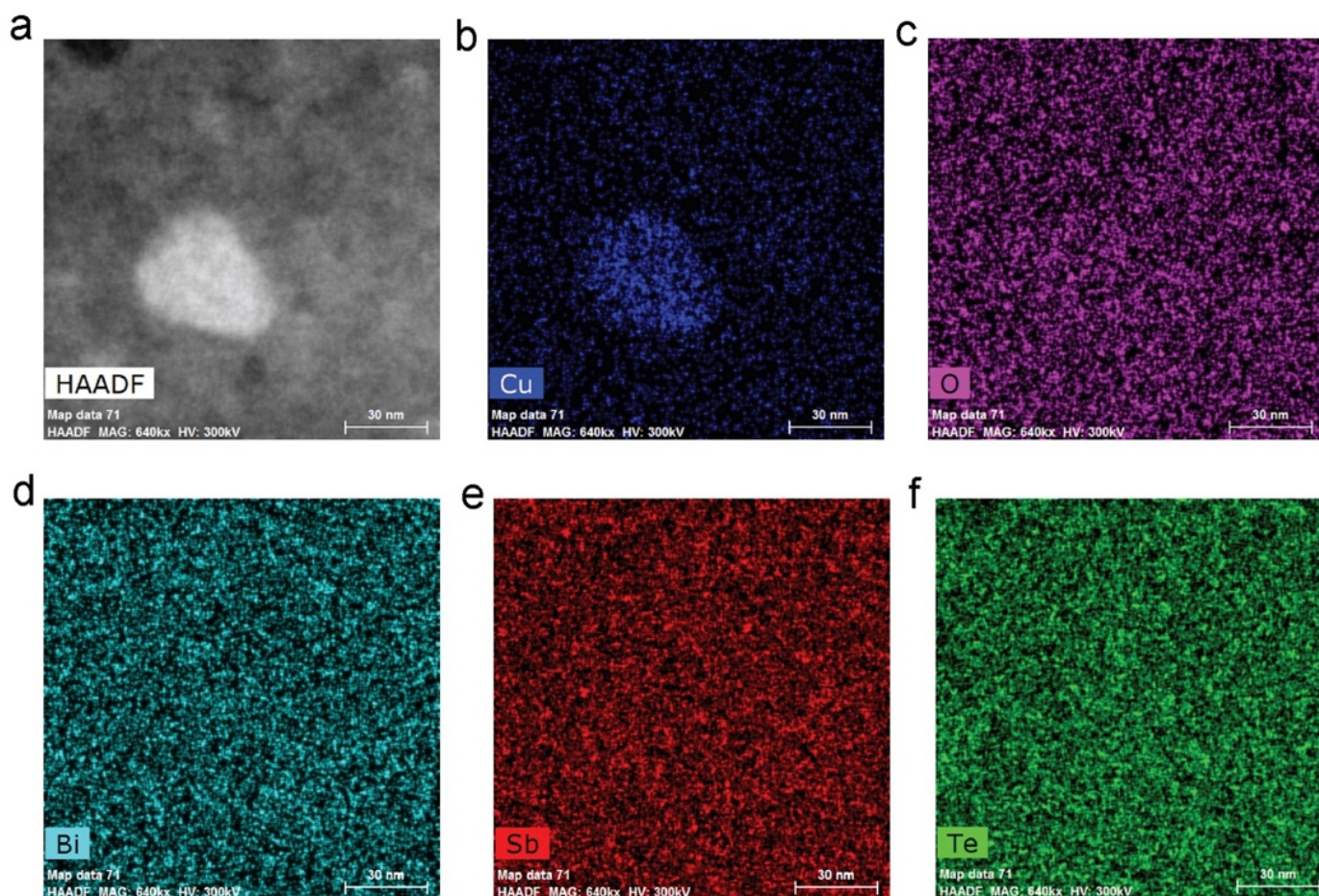

Fig. 3 HAADF-STEM image (a) and (b-f) EDS elemental mapping of the BiSbTe·0.3%CuO sample.

controlled within 0.08 W/(m·K) over a wide measurement temperature range (312~493 K). Therefore, there is a compromise between κ_e, κ_{lat} and κ_{bi}, where the increase of CuO concentration increases κ_e while lowering κ_{lat} and κ_{bi} simultaneously.

To explore the role of Cu and O doping using quantum mechanics, we have performed several DFT calculations, including spin-orbit coupling, which is necessary to reproduce the small energy gap that is measured experimentally. We found that Sb_2Te_3 and Bi_2Te_3 have very similar results and we therefore only discuss the results for the former. The possible doping defects from Cu and O are the substitution of Sb/Te atoms and the interstitial defects, respectively. The unit cell Energies of different compounds are listed in Table S2. The formation energies for all the defects are listed in Table 1. The calculation details are shown in Supplemental Information Section 4. The formation energy of different defects as a function of Cu chemical potential are plotted in Fig. S10. It is seen that the lowest-energy defects formed by Cu and O are the Cu substitution of Sb and the O interstitial defects, respectively.

Since it has been experimentally observed that Cu and O are separated after SPS and the hole concentration increases after CuO doping, we use DFT calculations to find out if these two kinds of defects can provide holes. We have calculated the projected densities of states (pDOS) for perfect Sb_2Te_3, Sb_2Te_3 with Cu_{Sb} defect, and Sb_2Te_3 with O interstitial defects as shown in Figs. 5a-c, respectively. The zero of energy is set at the top of the valence bands. It is clear that Cu doping introduces a substantial concentration of holes and the material remains semiconducting. The origin of p-type doping by substitutional Cu can be traced to the fact that, as shown in Fig. 5b, its ten $3d$ electrons lie deep inside the valence bands and its single $3s$ level spans the valence bands. Since Cu has an odd number of electrons and substitutes an atom with an even number of electrons, inevitably we end up with a hole concentration. Calculations of interstitial oxygen impurities again reveal that they dope the material p-type. As Fig. 5c shows, the $2p$ states of interstitial O lie deep in the valence bands. Since an O atom has only four $2p$ electrons and its $2p$ state, being within the valence bands, must be fully occupied with six electrons, it is inevitable that every interstitial O atom introduces two holes at the top of the valence bands. These results explain the observed enhanced p-type
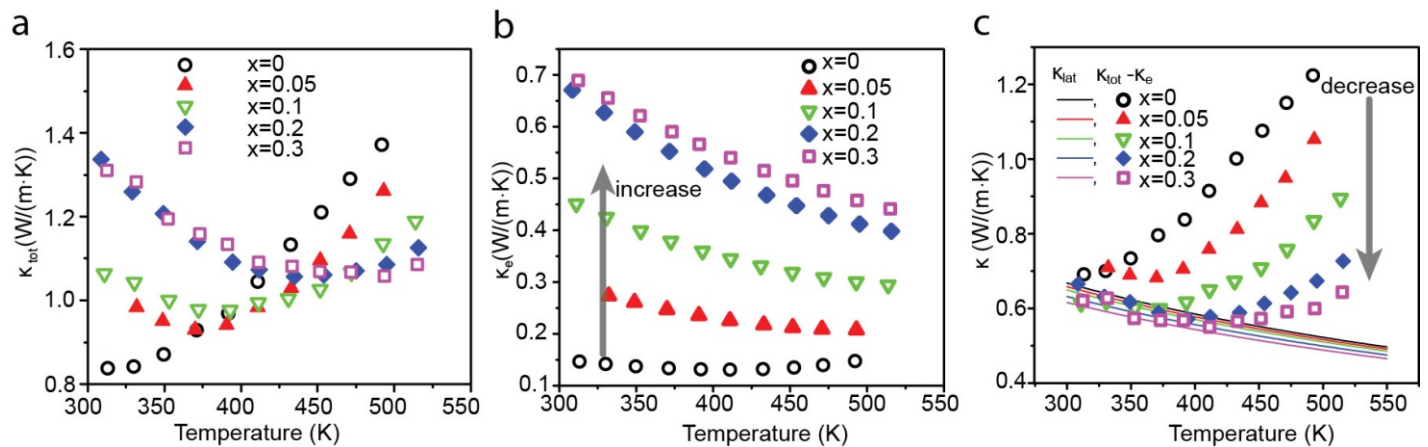

Fig. 4 Thermal conductivity of BiSbTe·x%CuO composites. (a) Total thermal conductivity κ_{tot} and (b) electronic thermal conductivity κ_e of BiSbTe·x%CuO composites; (c) Comparison of κ_{lat} and $\kappa_{tot} - \kappa_e$. The difference between them is the bipolar thermal conductivity contribution, which decreases with increasing CuO concentration as indicated by the thick downward grey arrow.

Table 1. The possible doping defects formed by Cu and O and their formation energies.

Possible doping mechanisms	Cu		O	
	Formation Energy	Provide holes?	Formation Energy	Provide holes?
Substitute Sb	**0.33 eV/atom**	**Yes**	2.37 eV/atom	Yes
Substitute Te	1.85 eV/atom	No	-0.50 eV/atom	No
Interstitial	0.85 eV/atom	No	**-1.40 eV/atom**	**Yes**

doping.

Benefiting from the effective p-doping from Cu and O, the figure of merit zT of BiSbTe·x%CuO nanocomposites is comprehensively improved, as presented in Fig. 5d. For pure BiSbTe, the zT over the entire measured temperature range is kept below 1.0 and decreases with measurement temperature. For BiSbTe·x%CuO with 0.05 %~0.3 % CuO concentration, the zT peak can reach 1.1~1.2, and the temperature for zT peak shows a dependence on the CuO concentration (Fig. S11). The temperature for zT peak was shifted from 317 K for pure BiSbTe to 377 K for BiSbTe·0.05%CuO, 395 K for BiSbTe·0.1%CuO, 452 K for BiSbTe·0.2%CuO and 475 K for BiSbTe·0.3%CuO. In addition, the zT can maintain a value above 1.0 over a wide temperature range. For example, zT of BiSbTe·0.1%CuO is over 1.0 from 330 to 474 K, which makes BiSbTe·x%CuO a very competitive thermoelectric material in solid-state cooling as well as waste heat recovery.

Additionally, owing to the superionic behavior in Cu-containing thermoelectric materials under an electrical load, the stability of Cu-containing thermoelectric materials remains a great concern.[34,35] Our BiSbTe·x%CuO composites show extremely good stability not only at inert atmosphere but also exposed to air. As shown in Fig. S12, the black plots correspond to the pristine electrical conductivity σ and Seebeck coefficient S of one BiSbTe·0.1%CuO sample. After the measurement, this sample was annealed at 475 K under argon atmosphere for 24 h, followed by the 2nd measurement of σ and S (red plots in Fig. 5b). It is found that both of σ and S do not change much. Furthermore, this sample was annealed for another 24 h at 475 K in air. The measurement results (green plots in Fig. S12) afterwards indicate that the sample is still stable and shows negligible change compared with its pristine state.

In summary, we for the first time realized effective doping of BiSbTe nanocomposites by metal oxide. Due to the remarkable increase of hole concentration and significant suppression of the bipolar effect,

the thermoelectric properties, especially the electrical conductivity and bipolar thermal conductivity, have been controllably modulated by a small concentration of CuO doping (0.05 %~0.3 %). Consequently, the figure of merit has been comprehensively optimized, capable of reaching above 1.0 over a wide temperature range. In addition, CuO doping exhibits excellent stability. This new approach opens up new opportunities and insights for improving and effectively controlling the thermoelectric performance by chemical doping.

Acknowledgment

Supporting Information

Supporting Information includes the experimental, characterization and theoretical modeling parts, 12 Figures and 2 tables.

References

1. X. Shi, L. Chen and C. Uher, *Int. Mater. Rev.,* 2016, **61**, 379-415.
2. T. Zhu, L. Hu, X. Zhao and J. He, *Adv. Sci.,* 2016, **3**, 160004.
3. H. J. Goldsmid, *Materials,* 2014, **7**, 2577-2592.
4. J. P. Heremans, B. Wiendlocha and A. M. Chamoire, *Energy Environ. Sci.,* 2012, **5**, 5510-5530.
5. J. Li, Q. Tan, J. F. Li, D. W. Liu, F. Li, Z. Y. Li, M. Zou and K. Wang, *Adv.*
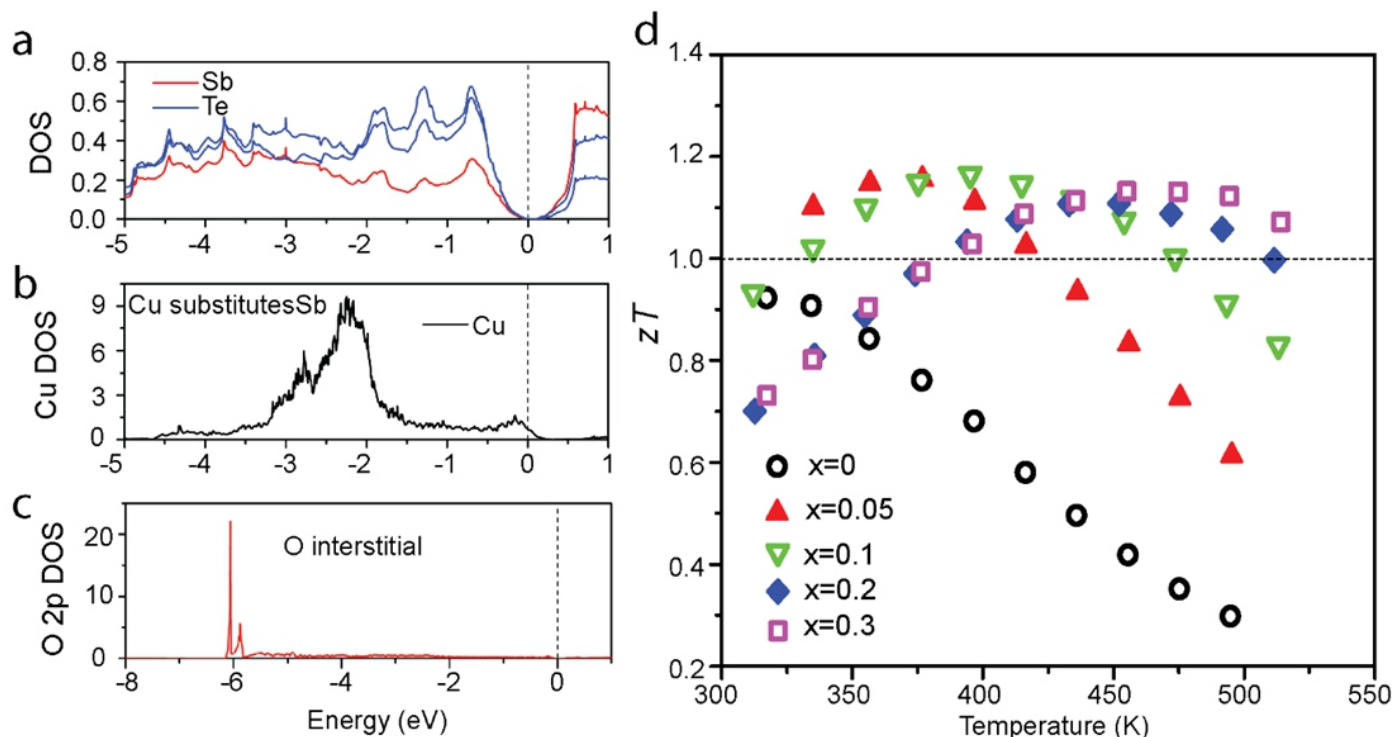

Fig. 5 DFT calculation and the figure of merit zT. Projected DOS for a perfect Sb_2Te_3 crystal; (a) and for an Sb_2Te_3 crystal doped with Cu substituting Sb (b); (c) The partial DOS of the 2p orbital of O as an interstitial defect in Sb_2Te_3 crystal; (d) Figure of merit zT of BiSbTe·x%CuO nanocomposites.

Func. Mater., 2013, **23**, 4317-4323.

6. S. I. Kim, K. H. Lee, H. A. Mun, H. S. Kim, S. W. Hwang, J. W. Roh, D. J. Yang, W. H. Shin, X. S. Li and Y. H. Lee, *Science,* 2015, **348**, 109-114.

7. T. Zhu, Y. Liu, C. Fu, J. P. Heremans, J. G. Snyder and X. Zhao, *Adv. Mater.,* 2017, **14**, 1605884.

8. L. Yang, Z. G. Chen, M. S. Dargusch and J. Zou, *Adv. Energy Mater.*, 2017, **8**, 1701797.

9. B. Xu, T. Feng, Z. Li, W. Zheng and Y. Wu, *Adv. Mater.* 2018, e1801904.

10. Z. Chen, X. Zhang and Y. Pei, *Adv. Mater.* 2018, **30**, e1705617.

11. S. Lin, W. Li, S. Li, X. Zhang, Z. Chen, Y. Xu, Y. Chen and Y. Pei, *Joule,* 2017, **1**, 816–830.

12. Z. Chen, B. Ge, W. Li, S. Lin, J. Shen, Y. Chang, R. Hanus, G. J. Snyder and Y. Pei, *Nat. Commun.,* 2017, **8**, 13828.

13. F. Hao, P. Qiu, Q. Song, H. Chen, P. Lu, D. Ren, X. Shi and L. Chen, *Materials,* 2017, **10**, 251.

14. Y. Pan, U. Aydemir, F. H. Sun, C. F. Wu, T. C. Chasapis, G. J. Snyder and J. F. Li, *Adv. Sci.,* 2017, **4**, 1700259.

15. B. Xu, M. T. Agne, T. Feng, T. C. Chasapis, X. Ruan, Y. Zhou, H. Zheng, J. H. Bahk, M. G. Kanatzidis, G. J. Snyder and Y. Wu, *Adv. Mater.,* 2017, **29**, 1605140.

16. J. Horák, L. Tichy, P. Lostak and A. Vasko, *Cryst. Lattice Defects,* 1976, **6**, 233-238.

17. Q. Zhang, X. Ai, L. Wang, Y. Chang, W. Luo, W. Jiang and L. Chen, *Adv. Func. Mater.,* 2015, **25**, 966-976.

18. A. Banik, B. Vishal, S. Perumal, R. Datta and K. Biswas, *Energy Environ. Sci.,* 2016, **9**, 2011-2019.

19. C. Ou, J. Hou, T. R. Wei, B. Jiang, S. Jiao, J. F. Li and H. Zhu, *NPG Asia Mater.,* 2015, **7**, e182.

20. S. Ortega, M. Ibáñez, Y. Liu, Y. Zhang, M. V. Kovalenko, D. Cadavid and A. Cabot, *Chem. Soc. Rev.,* 2017, **46**, 3510-3528.

21. H. Ohta, K. Sugiura and K. Koumoto, *Inorg. Chem.,* 2008, **47**, 8429-8436.

22. K. Koumoto, Y. Wang, R. Zhang, A. Kosuga and R. Funahashi, *Annu. Rev. Mater. Res.,* 2010, **40**, 363-394.

23. T. Zhang, Q. Zhang, J. Jiang, Z. Xiong, J. Chen, Y. Zhang, W. Li and G. Xu, *Appl. Phys. Lett.* 2011, **98**, 022104.

24. Y. Li, G. Liu, X. Qin and F. Shan, *RSC Adv.,* 2016, **6**, 112050-112056.

25. B. Madavali, H. S. Kim, K. H. Lee and S. J. Hong, *J. Appl. Phys.,* 2017, **121**, 225104.

26. J. Bludská, I. Jakubec, Č. Drašar, P. Lošťák and J. Horák, *J. Philos. Mag.,* 2007, **87**, 325-335.

27. H. J. Yu, M. Jeong, Y. S. Lim, W. S. Seo, O. J. Kwon, C. H. Park and H. J. Hwang, *RSC Adv.,* 2014, **4**, 43811-43814.

28. H. J. Wu and W. T. Yen, *Acta Mater.,* 2018, **157**, 33–41.

29. K. Biswas, J. He, I. D. Blum, C. I. Wu, T. P. Hogan, D. N. Seidman, V. P. Dravid and M. G. Kanatzidis, *Nature,* 2012, **489**, 414-418.

30. G. Han, Z. G. Chen, L. Yang, M. Hong, J. Drennan and J. Zou, *ACS Appl. Mater. Interfaces,* 2014, **7**, 989-995.

31. Y. Zheng, Q. Zhang, X. Su, H. Xie, S. Shu, T. Chen, G. Tan, Y. Yan, X. Tang, C. Uher and G. J. Snyder, *Adv. Energy Mater.,* 2015, **5**, 1401391.

32. J. H. Bahk and A. Shakouri, A. *Phys. Rev. B,* 2016, **93**, 165209.

33. G. J. Snyder and E. S. Toberer, *Nat. Mater.,* 2008, **7**, 105-114.

34. G. Dennler, R. Chmielowski, S. Jacob, F. Capet, P. Roussel, S. Zastrow, K. Nielsch, I. Opahle and G. K. H. Madsen, *Adv. Energy Mater.*, 2014, **4**, 1301581.

35. H. Liu, X. Shi, F. Xu, L. Zhang, W. Zhang, L. Chen, Q. Li, C. Uher, T. Day and G. J. Snyder, *Nat. Mater.,* 2012, **11**, 422-425.